Electronic Supplementary Information

Tuning the Modal Coupling in Three-Dimensional Au@Cu_2O@Au Core-Shell-Satellite Nanostructure for Enhanced Plasmonic Photocatalysis

Yahui Yang[a], Binbin Zhang[a], Xuehao Sun[a], Yunlong Tao[a], Guizeng Yang[a], Chuang Liu[a], Zixu Wang[a], Lichao Sun*[a,b], and Qingfeng Zhang*[a]

[a] College of Chemistry and Molecular Sciences, Hubei Key Laboratory of Electrochemical Power Sources, Wuhan University, Wuhan 430072, China

[b] Suzhou Institute of Wuhan University, Suzhou 215123, China

*To whom correspondence should be addressed.

Email: lichaosun@whu.edu.cn (L. S.)

Email: zhangqf@whu.edu.cn (Q. Z.)

Table of Contents

S1. Additional Experimental Details

S1.1 Chemicals and Materials

Gold(III) chloride trihydrate ($HAuCl_4 \cdot 3H_2O$, 99%), sodium borohydride ($NaBH_4$, 99%), L-ascorbic acid (AA, 99.9%), potassium iodide (KI, >99%), N_2H_4 solution (35 wt %), and 4-Nitrothiophenol (4-NTP, 99%) were obtained from Sigma-Aldrich. Silver nitrate ($AgNO_3$, 99.9995% metals basis) and polyvinyl pyrrolidone (PVP, M.W. 58000 were obtained from Alfa Aesar. Cetyltrimethylammonium bromide (CTAB, >98%), cetyltrimethylammonium chloride (CTAC, >98%), and sodium oleate (NaOL, >97%) were purchased from TCI. Hydroxylamine hydrochloride ($NH_3OH \cdot Cl$, 99.99% metals basis) and sodium sulfate (Na_2SO_4, 99%) were obtained from Meryer. Cupric chloride ($CuCl_2$, 99.99% metals basis), Copper(ii) nitrate hydrate ($Cu(NO_3)_2 \cdot 3H_2O$, 99.99%), and sodium dodecyl sulfate (SDS, >99%) were obtained from Aladdin. L-cysteine-phenylalanine (L-CYP, >98%) and D-cysteine-phenylalanine (D-CYP, >98%) were purchased from Sangon Biotechnology. All reagents were used as received without further purification. Millipore ultrapure water (18.2 MΩ resistivity) was used for all experiments.

S1.2 Synthesis of Single-crystalline Au Nanoparticles (NPs): Rhombicuboctahedron (RCO)

S1.2.1 Synthesis of Au Seeds. Single-crystalline Au NPs with different morphologies were synthesized using a previously published seed-mediated growth method with slight modifications.[1] For the synthesis of single-crystalline Au NPs, colloidal Au seeds were prepared at first by reducing $HAuCl_4$ with $NaBH_4$ in the presence of CTAC. Typically, 100 µL of 25 mM $HAuCl_4$ was mixed with 5 mL of 0.2 M CTAC solution and 4.9 mL of water. Then, 450 µL of ice-cold, freshly prepared 20 mM $NaBH_4$ was quickly injected into the mixture under magnetic stir. The seed solution was stirred for 2 min and then left undisturbed for 1 hour at 30 °C.

S1.2.2 Synthesis of Au RCO. For the Au NPs growth solution, two vials labeled A and B containing the same composition were first prepared. The vials were then kept in a water bath set at 30 °C. For the synthesis of Au RCO: to both vials were added 5 mL of 0.2 M CTAC, 4.595 mL of water, 100 µL of 25 mM $HAuCl_4$ solution, and 30 µL of 1 mM KI in sequence. Finally, 220 µL of 40 mM AA was introduced to the vials for synthesis. The total volume of solution in each vial was set to 10.0 mL. Next, 55 µL of the Au seed solution was added to the growth solution in vial A with shaking until the solution color turned light red (~10 s). Then 55 µL of the solution in vial A was transferred to vial B with thorough mixing for ~20 s. The solution in vial B was left undisturbed for 15 min at 30 °C for particle growth. The products were collected by centrifugation and re-dispersed in 1 mL of 1 mM CTAB for further use.

S1.3 Synthesis of Au Nanorods (NRs)

Au NRs were synthesized using a previously published seed-mediated growth protocol[2, 3] with minor modifications. Colloidal Au seeds were prepared by reducing $HAuCl_4$ with $NaBH_4$ in the presence of CTAB. First, 5.0 mL of 0.5 mM $HAuCl_4$ was mixed with 5.0 mL of 200 mM CTAB solution. Then, 1.0 mL of ice-cold, freshly prepared 6.0 mM $NaBH_4$ was quickly injected into the mixture under magnetic stir (1200 rpm). The seed solution was stirred for 2 min and then left undisturbed for 30 min before use. To prepare the Au NRs growth solution, 7.0 g of CTAB and 1.234 g of NaOL were dissolved in 250 mL of water at 60 °C. The solution was cooled to 30 °C and then 36 mL of 4.0 mM $AgNO_3$ was added. The mixture was kept undisturbed at 30 °C for 15 min, followed by the addition of 250 mL of 1 mM $HAuCl_4$. The solution became colorless after being stirred at 700 rpm for 90 min and 2.2 mL of HCl (37 wt % in water, 12.1 M) was then introduced into the mixture. After another 15 min of a slow magnetic stir at 400 rpm, 1.25 mL of 64 mM AA was added. Finally, 4.0 mL of seed solution was injected into the growth solution and the mixture solution was vigorously stirred for another 30 s and then left undisturbed at 30 °C for 12 h. The resulting Au NRs were collected by centrifugation at 7000 rpm for 20 min followed by removal of the supernatant and finally re-dispersed in 30 mL of 100 mM CTAB.

S1.4 Chiral Au Rhombic Dodecahedron (RD)

Chiral Au RDs were prepared through the overgrowth of single-crystalline Au RD in the presence of $HAuCl_4$, CTAB, AA, and L/D-CYP.[4] In a typical procedure, 1 mL of Au RD was first re-dispersed in 1 mL of 1 mM CTAB after being washed twice with water and used as seeds. The growth solution was prepared by sequentially adding H_2O (3.116 mL), $HAuCl_4$ (100 μL, 10 mM), and AA (960 μL, 0.10 M) into a CTAB (0.8 mL, 0.10 M) solution. After gently mixing the growth solution for 30 s, 4 μL of 0.1 mM D-CYP solution was added followed by a gentle mixing for 30 s. The growth of chiral Au RDs was initiated by adding 20 μL of Au seeds. The reactants were gently mixed for 30 s immediately after the addition of Au seeds and then left undisturbed at 30 °C for 2 h in a water bath. The obtained Au CRD NPs were centrifuged under 3000 rpm for 5 min to remove unreacted reagents and were re-dispersed in a CTAB (1 mL,1 mM) solution for further use. The opposite chiral structure is achieved by substituting the configuration of the chiral molecule (L/D-CYP).

S1.5 Synthesis of Au@Cu_2O NPs

The Au@Cu_2O NPs with an average diameter of ~145 nm were synthesized following a one-step overgrowth method. Typically, 80 μL of colloidal Au RCO NPs was first introduced into 5 mL of 2 wt % PVP aqueous solution. Then, various amounts (2.5-100 μL) of 0.1 M $Cu(NO_3)_2$ solution, depending on the desired thickness of the resulting Cu_2O shells, were subsequently added. Then 11.2 μL of 5 M NaOH and 5 μL of N_2H_4 solution (35 wt %) were added under magnetic stir. The solutions were kept stirring for 30 min and the resulting core-shell NPs were subsequently separated from the reaction mixtures by centrifugation. All the reactions are conducted in the ice bath. All Au@Cu_2O NPs were washed with water and anhydrous ethanol and finally redispersed in ethanol for storage and further use. Chiral Au RD@Cu_2O NPs were synthesized using chiral Au RD as seeds instead of Au RCO.

S1.6 Synthesis of Au@Cu_2O NRs

The Au@Cu_2O NRs were synthesized according to the method for the preparation of Au@Cu_2O NPs except for using Au NRs as the starting seeds. In a typical procedure, 100 μL of Au NRs (extinction peak at ~715 nm) and $CuCl_2$ (0.1 M, 40 μL) were first added into 10 mL of 8.7 wt % SDS aqueous solution. NaOH (5.0 M, 73 μL) and $NH_2OH\cdot HCl$ (0.1 M, 320 μL) were subsequently added under magnetic stir. After the mixture solution was subjected to gentle shaking for 15 s, it was left undisturbed at room temperature for 1 h. Centrifugation was finally performed on the mixture solution at 7500 rpm for 5 min. The resultant precipitate was washed with water several times and eventually redispersed and kept in ethanol for further use. The thickness of the Cu_2O shell can be adjusted by varying the volume of the added $CuCl_2$ solution or Au seeds.

S1.7 Synthesis of Au@Cu_2O@Au (ACA) NPs and NRs

S1.7.1 ACA NPs. In the case of synthesis of ACA NPs, the Au@Cu_2O NPs were firstly dissolved in 1 mL deionized water, and then, 0.0, 0.1, 0.3, 0.5, 0.7, 1.0, 1.2, 1.5, 1.7 mM of 0.5 mL $HAuCl_4$ aqueous solution were respectively added to the samples and labeled I, II, III, IV, V, VI, VII, VIII and IX. The mixture solution was subjected to manual gentle shaking for 60 s. The resulting ACA NPs were collected by centrifugation at 7000 rpm for 5 min followed by removal of the supernatant and finally re-dispersed in 1 mL of 1 mM CTAB for further use.

S1.7.2 ACA NRs. In the case of synthesis of ACA NRs, the Au@Cu_2O NRs were firstly dissolved in 5 mL 2 wt % PVP aqueous solution, and then were washed with anhydrous ethanol twice. The Au@Cu_2O NRs were dissolved in 1 mL deionized water, and then, 0.0, 0.1, 0.3, 0.5, 0.7, 1.0, 1.2, 1.5, 1.7 mM of 0.2 mL $HAuCl_4$ aqueous solution were respectively added to the samples and labeled I, II, III, IV, V, VI, VII, VIII and IX. The mixture solution was subjected to manual gentle shaking for 60 s. The resulting ACA NRs were collected by centrifugation at 7000 rpm for 5 min followed by removal of the supernatant and finally re-dispersed in 1 mL of 1 mM CTAB for further use.

S1.8 Characterization

The optical extinction spectra of the nanoparticles were measured on aqueous colloidal suspensions at room temperature using a Shimadzu UV-2600i spectrophotometer. The morphologies and structures of the nanoparticles were characterized by scanning electron microscopy (SEM) using Zeiss Merlin Compact and Zeiss GeminiSEM 500 field emission scanning electron microscopes. The samples for SEM were dispersed in water and drop-dried on silicon wafers. Transmission electron microscopy (TEM) images were obtained with a JOEL JEM-2100 Plus transmission electron microscope operated at an accelerating voltage of 200 kV. All samples for TEM measurements were dispersed in water and drop-dried on 300 mesh Formvar/carbon-coated Cu grids. X-ray diffraction (XRD) patterns of samples were obtained using Rigaku SmartLab SE, manufactured by Rigaku Corporation.

S1.9 Single-Particle Dark-Field Scattering Spectroscopy

Scattering spectra were collected using a home-built dark-field microscope based on an inverted microscope body (Zeiss AxioObserver m1) with a hyperspectral detection system. Unpolarized light generated from a tungsten-halogen lamp was focused onto the samples on indexed ITO glass substrates using a dark-field oil-immersion condenser (Zeiss, numerical aperture (NA) = 1.4) to create a total internal reflection excitation condition. The scattered light was collected with a 50× air-space objective lens (Zeiss, NA = 0.8) and passed to a hyperspectral detection system consisting of an imaging spectrograph with a slit aperture (Princeton Instrument, Acton SpectraPro 2150i with a Pixis 400 thermoelectrically cooled back-illuminated CCD camera) mounted on a computer-controlled translation stage (Newport Linear Actuator model LTA-HL).

S1.10 Time-resolved Surface-enhanced Raman Scattering (SERS) Measurements and the Analysis of Kinetic Results

S1.10.1 Time-resolved SERS measurements of the plasmon-driven photochemical transformation of 4-NTP using ACA NPs. The ACA NPs served as both the plasmonic photocatalysts and the SERS substrates. In a typical procedure, silicon substrates were cleaned in a piranha solution (H_2SO_4:H_2O_2, 7:3 volume ratio) for 15 min and then immersed in water to remove the excess acid. The silicon substrates were thoroughly rinsed with ethanol and dried with N_2 gas before use. The ACA NPs were incubated in 4-NTP solution with various concentrations at room temperature for 1 h and then washed with ethanol and redispersed in water. The 4-NTP-coated ACA NPs were drop-dried on silicon wafers for SERS measurements. Time-resolved SERS spectra were collected by using a HORIBA XploRA PLUS Raman microscope under 638 nm continuous wave (CW) laser excitation in the confocal mode (focal area of 2 μm diameter). A 50× objective (NA = 0.5) was used for Raman signal collection. The laser power focused on the samples was adjusted in the range of 100-1000 μW by using a neutral density filter, and the spectrum acquisition time was varied from 0.6 to 2 s under most experimental conditions.

S1.10.2 Analysis of Kinetic Results. The analysis of kinetic results followed the method developed in previous work with minor modifications.[5] The 4-NTP molecules adsorbed on Au surfaces underwent a reductive coupling process to form 4,4'-dimercaptoazobenzene (DMAB) following an apparent first-order rate law. We monitored the reaction progress in real-time based on the temporal evolution of the SERS spectral features. Because of the large differences in the intrinsic Raman cross-sections of DMAB and 4-NTP and signal enhancements of various Raman vibrational modes, the apparent fractions of 4-NTP and DMAB, denoted as θ_{NTP} and θ_{DMAB}, respectively. We quantified the temporal evolutions of θ_{DMAB} and θ_{NTP} based on the relative intensities of the SERS peaks at 1438 cm^{-1} (N=N stretching mode) and 1338 cm^{-1} (nitro stretching mode), respectively, with respect to the SERS peak at 1572 cm^{-1} (benzene ring stretching mode). The plasmon-driven oxidative coupling of 4-ATP adsorbed on ACA NPs gave rise to nearly 100 % conversion of 4-ATP into DMAB (Figure S15). Therefore, the intensity ratio of the 1438 cm^{-1} mode to the 1572 cm^{-1} mode for DMAB on ACA NPs, denoted as R_{DMAB}, was used as an internal reference for the calculation of θ_{DMAB} at a reaction time, *t*, using the following equation:

$$\theta_{DMAB}(t) = \frac{I_{1438cm^{-1}}(t)/I_{1572cm^{-1}}(t)}{R_{DMAB}} \qquad \text{(Equation S1)}$$

Similarly, we used the peak intensity ratio of the 1338 cm^{-1} mode to the 1572 cm^{-1} mode for pure 4-NTP on ACA NPs, denoted as R_{NTP}, as an internal reference for the calculation of θ_{NTP}. The pure DMAB on Au@Cu_2O NSs@Au also had a spectral feature at 1338 cm^{-1} overlapping with the characteristic nitro stretching mode of 4-NTP. Therefore, the peak intensity ratio of the 1338 cm^{-1} mode to the 1572 cm^{-1} mode for pure DMAB on ACA NPs, denoted as Q_{DMAB}, was subtracted when calculating θ_{NTP} as shown below:

$$\theta_{NTP}(t) = \frac{I_{1338cm^{-1}}(t)/I_{1572cm^{-1}}(t) - \theta_{DMAB}(t)\times Q_{DMAB}}{R_{NTP}} \qquad \text{(Equation S2)}$$

The rate constants were obtained by performing least squares curve fitting to the experimentally measured θ_{DMAB} and θ_{NTP} trajectories using the first-order rate equations shown below:

$$\theta_{DMAB}(t) = \theta_{t=\infty}(t) \times (1 - e^{-kt}) \qquad \text{(Equation S3)}$$

$$\theta_{NTP}(t) = 1 - \theta_{t=\infty} + \theta_{t=\infty} \times e^{-kt} \qquad \text{(Equation S4)}$$

Where k is the apparent first-order rate constant and $\theta_{t=\infty}$ is the maximal reaction yield achievable at an infinitely long reaction time, respectively.

S1.11 Photocurrent Measurements

The measurements of photocurrent were carried out in a three-electrode, single-compartment quartz cell. All the experiments were performed at room temperature in 0.5 M Na_2SO_4 electrolyte (100 mL, pH = 6.6) deoxygenated using an Ar stream. The working electrode was prepared by depositing the as-prepared ACA NPs on Indium tin oxide (ITO) glass (1 cm^2 in deposition area). The 200 μL ethanol suspension of samples containing the same amount for the deposition. The counter and reference electrodes were platinum gauze and Ag/AgCl. The photocurrents were collected by an electrochemical analyzer CHI 660D by a fixed biased potential of -0.3 V (vs. Ag/AgCl) (or Linear sweep voltammetry by -0.2 to -1.0 V) at a sweep rate of 10 mV/s under chopped irradiation of a 300-W Xe lamp (λ > 400 nm, Solaredge 700, the power density of light was 400 $mW \cdot cm^{-2}$, light on/off cycles: 6 s).

S1.12 Transient Absorption (TA) Spectroscopy

A femtosecond pump-probe TA spectroscopic measurements were performed on the ACA NPs. A 70 fs pump laser at the fixed wavelength excited the samples, and a broadband probe was delayed at various times to monitor the reflection spectrum. The spectral change ΔA was obtained by comparing the absorption spectroscopy after and before pump pulse excitation. In experiments, a Ti:sapphire laser system (800 nm, 1 kHz, 6 mJ/pulse, Coherent), nonlinear frequency mixing techniques, and a transient absorption spectrometer (TA 100, Ultrafast Spectra LLC) at room temperature. The output pulse generated from the regenerative amplifier was split into two beams. One part of the 800 nm output laser was used to pump a noncollinear OPA to produce a wavelength-tunable laser pulse as pump-probe. Another weak part was used to make a broad probe beam (550-950 nm) by focusing on a sapphire crystal. The pump and probe beams were focused with a parabolic reflector and overlapped on the sample. A variable neutral-density filter wheel was used to control the power of the pump pulse. The power of the pump pulse was fixed at 90 μW in experiments. The instrument response function (IRF) of our system was estimated by measuring solvent responses.

The ultrafast kinetics for Au@Cu_2O and ACA NPs after 450 nm excitation in the main text (Figure 6) were fitted to single exponential rise and decay. The electron-electron scattering in gold is fast and occurs within the rise time of the measured transient signal. The electron dynamics of Au NPs can be fitted by the exponential function convoluted by instrument response as the following equations.

$$\Delta R = s(t)\{IRF \otimes [a_1 exp(-t/\tau_{e-ph}) - a_2 exp(-t/\tau_{e-e})]\} \quad \text{(Equation S5)}$$

where ΔR is the bleach signal, s(t) is the step function, IRF is the instrument response function, and τ_{e-ph} and τ_{e-e} are the electron-phonon scattering and electron-electron scattering times, respectively. a_1 and a_2 are the amplitudes constants of the exponential components. The fitting results are shown in Figure 6 in the main text.

S1.13 Derivation of the Dipole Moment Formula for Spherical Core-Shell NPs

For metal-semiconductor core-shell NPs, the calculation of the dipole moment is based on the theory of electrostatics. In a uniform external electric field, the core-shell NPs will be polarized, generating an induced dipole moment. We assume that the radius of the metal core is R_1, the outer radius of the semiconductor shell is R_2, the dielectric constant of the metal is ε_1, the dielectric constant of the semiconductor is ε_2, and the dielectric constant of the surrounding medium is ε_0. By using the boundary conditions of the electrostatic field (the continuity of the electric field intensity $\vec{E}$ and the electric displacement vector $\vec{D} = \varepsilon\vec{E}$ at the interface) and the method of separation of variables to solve Laplace's equation $\nabla^2\varphi = 0$ (φ is the electric potential).

For the external region ($r > R_2$), the electric potential φ_{out} can be expressed as:

$$\varphi out = -E_0 r\cos\theta + \frac{P}{4\pi\varepsilon 0 r^2}\cos\theta \qquad \text{(Equation S6)}$$

where E_0 is the intensity of the external electric field, θ is the angle between the position vector and the direction of the external electric field, and P is the dipole moment we want to calculate.

In the semiconductor shell layer ($R_1 < r < R_2$), the electric potential φ_{shell} is

$$\varphi_{shell} = A_1 r\cos\theta + \frac{A_2}{r^2}\cos\theta \qquad \text{(Equation S7)}$$

Inside the metal core ($r < R_1$), since the metal is an equipotential body, $\varphi_{in} = C$ (a constant)

According to the boundary conditions $\varphi_{in}(R_1) = \varphi_{shell}(R_1)$, $\varepsilon_2\frac{\partial\varphi_{shell}}{\partial r}(R_1) = \varepsilon_1\frac{\partial\varphi_{in}}{\partial r}(R_1) = 0$ (the electric field inside the metal is 0)

$$\varphi_{shell}(R_2) = \varphi_{out}(R_2),\ \varepsilon_0\frac{\partial\varphi_{out}}{\partial r}(R_2) = \varepsilon_2\frac{\partial\varphi_{shell}}{\partial r}(R_2) \qquad \text{(Equation S8)}$$

By solving the system of equations composed of the above boundary conditions, we can obtain the expression of the dipole moment P:

$$P = 4\pi\varepsilon_0 E_0\frac{\varepsilon_2-\varepsilon_0}{\frac{\varepsilon_0-\varepsilon_1}{\varepsilon_2+2\varepsilon_1}R_1^3+\frac{\varepsilon_2+2\varepsilon_0}{3}(R_2^3-R_1^3)}R_2^3 \qquad \text{(Equation S9)}$$

Note that it is difficult to directly correlate thickness changes with optical changes of ACA NPs according to the revised expression of P_{cavity} (Equation S9). However, we can qualitatively understand the optical variation with the change in Cu_2O shell thickness. As shown in Figure S12D, we can't observe the obvious optical variation of ACA according to the ensemble extinction spectra when the Cu_2O thickness of Au@Cu_2O is relatively large (>70 nm). The phenomenon can also be regarded that the cavity with relatively thick Cu_2O is less sensitive to the variation of plasmon dipole. As shown in Figure 3D, the shade of the color represents the degree of spectral variation. However, if Cu_2O is relatively thin, the cavity is more sensitive to the plasmon dipole, showing more obvious spectral variation. Notably, the thickness term in the equation "P_{cavity}" is simply to indicate that the thickness of Cavity plays an important role in coupling and the simplified model (the interaction between two asymmetric dipoles) is more convenient to understand.

S2. Additional Figures and Tables

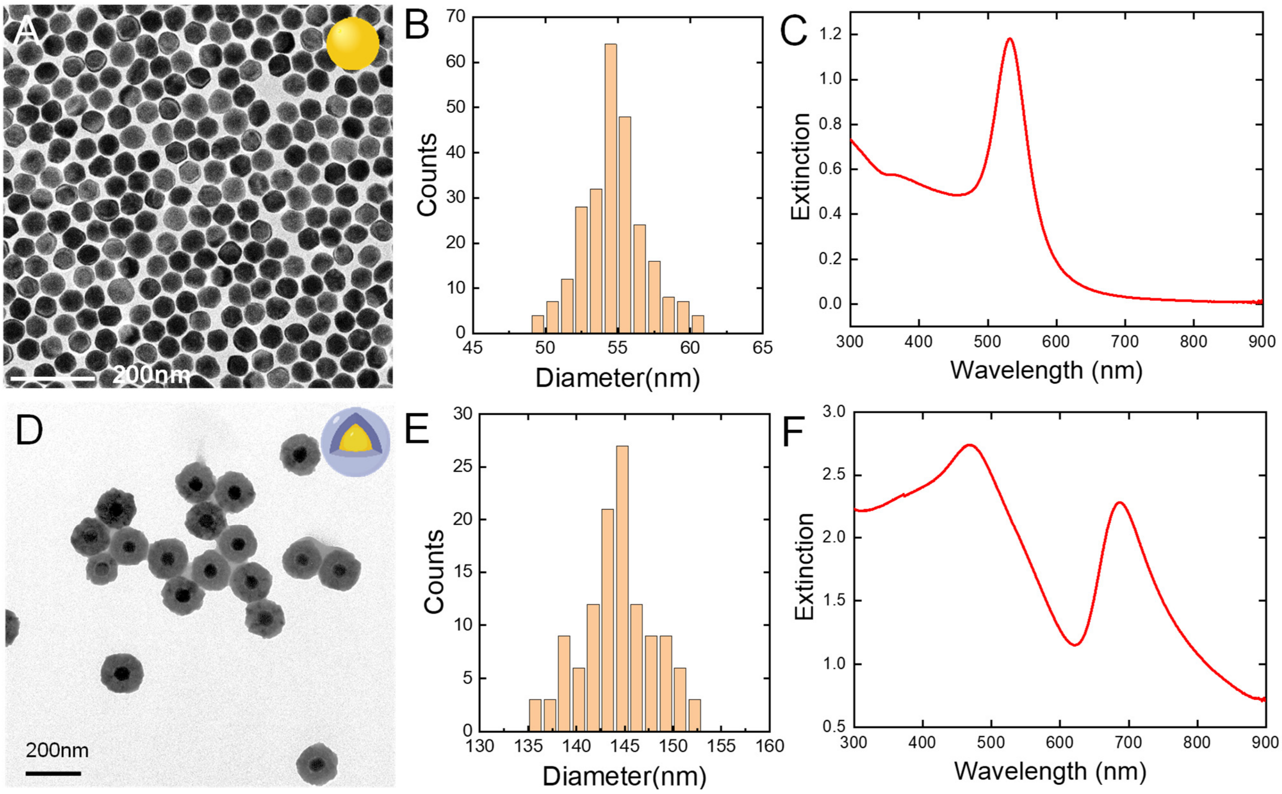

Figure S1. (A) TEM image of single-crystalline Au RCO NPs. (B) Histogram showing the size distribution of Au RCO NPs. (C) Optical extinction spectrum of Au RCO NPs in water. (D) TEM image of Au@Cu_2O NPs. (E) Histogram showing the size distribution of Au@Cu_2O NPs. (F) Optical extinction spectrum of Au@Cu_2O NPs in water.

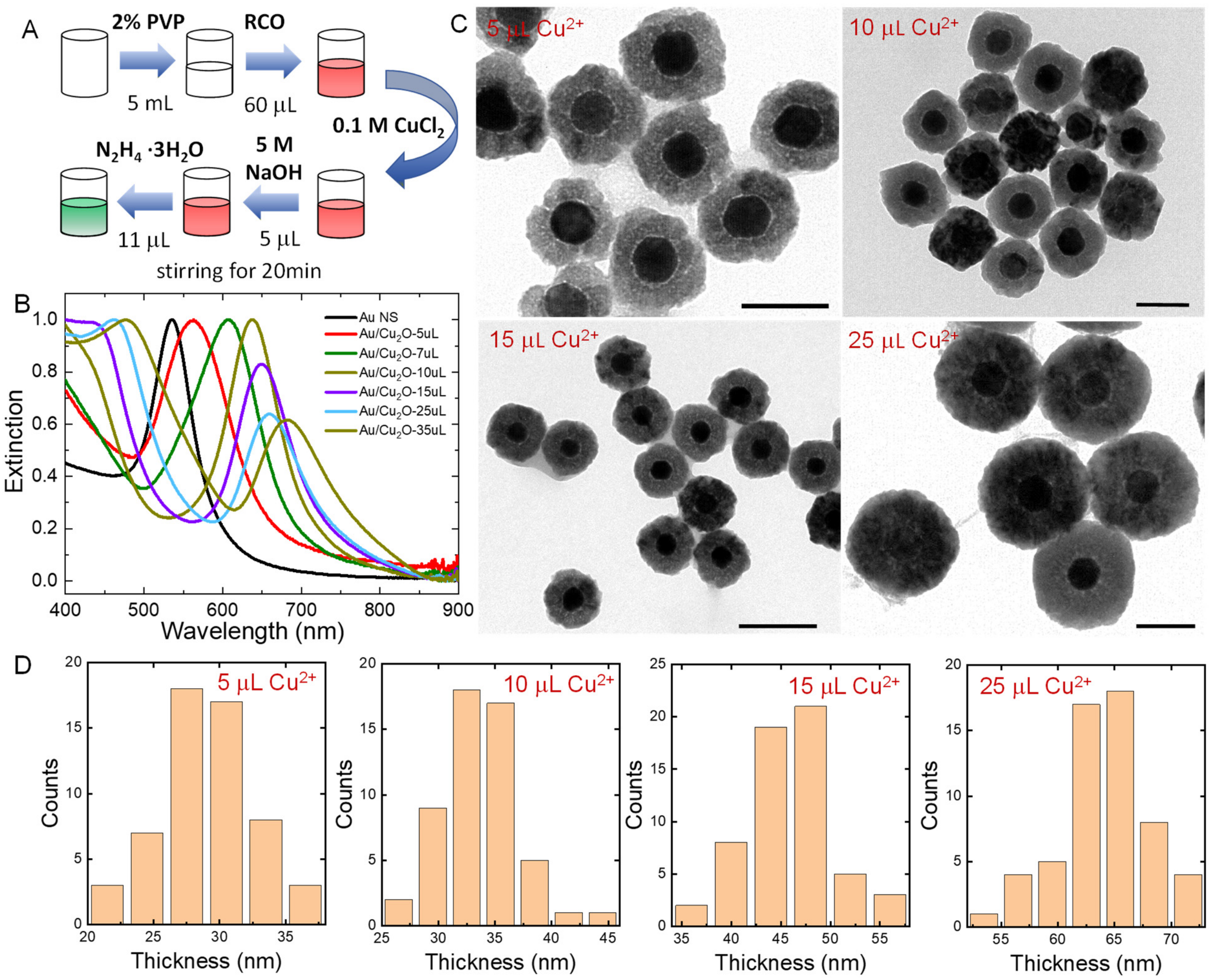

Figure S2. (A) Schematic illustration of the procedure used to synthesize Au@Cu_2O NPs with various thicknesses of Cu_2O shell. (B) Normalized optical extinction spectrum of Au@Cu_2O with different thicknesses of Cu_2O shell in water. (C) TEM images of Au@Cu_2O NPs synthesized using different concentrations of $CuCl_2$ precursor corresponding to Figure B. Scale bars: 100 nm. (D) Histogram of Cu_2O thickness as a function of the amount of Cu^{2+} precursor as indicated in each panel.

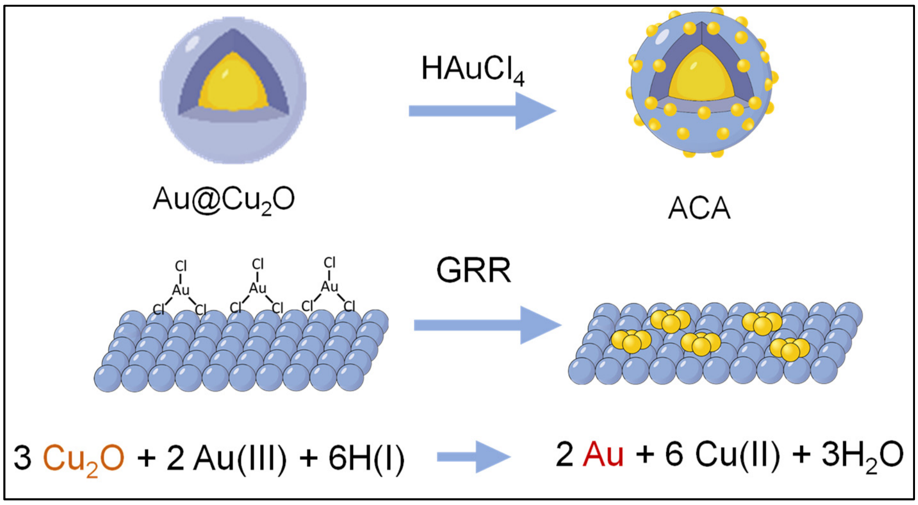

Figure S3. Schematic illustration of the construction of the ACA nanostructures by reacting the Cu_2O shell with $HAuCl_4$ through a galvanic replacement reaction (GRR) process.

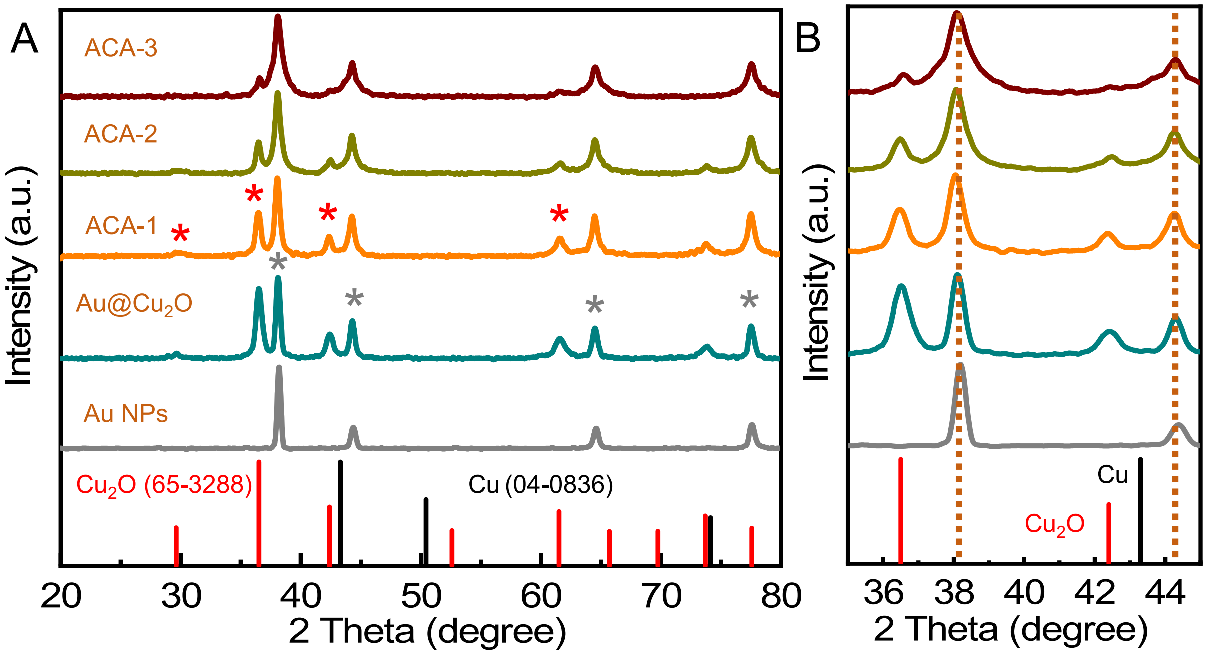

Figure S4. (A) XRD patterns of Au, Au@Cu_2O, and ACA NPs. The amount of $HAuCl_4$ increases from ACA-1 to ACA-3. The emerging diffraction peaks located at 38.19°, 44.39°, 64.58°, and 77.62° can be indexed to the Au (JCPDS: 65-2870), which correspond to the (111), (200), (220), and (311) planes of face-center cubic (fcc) Au. The diffraction peaks located at 29.55°, 38.18°, 42.30°, 61.34°, and 73.53° can be indexed as Cu_2O component. Notably, close examination shows that the ratio of the intensity of the (111) peak of Au to that of the (*111) peak of Cu_2O increases with increasing amounts of $HAuCl_4$, indicating the continuous growth of Au satellites on Cu_2O NPs and the decrease of the intensity of Cu_2O peaks are mainly caused by the etching of Cu_2O during the process of GRR. Moreover, none of the Cu^0 elements and CuAu alloy phase were observed in the XRD patterns of ACA NPs. The formation of Cu-Au alloy would lead to the redshift of the (111) peak, however, it was not observed in our case. XRD patterns of the Cu_2O component (JCPDS: 65-3288) and Cu (JCPDS: 04-0836) are also included for comparison.

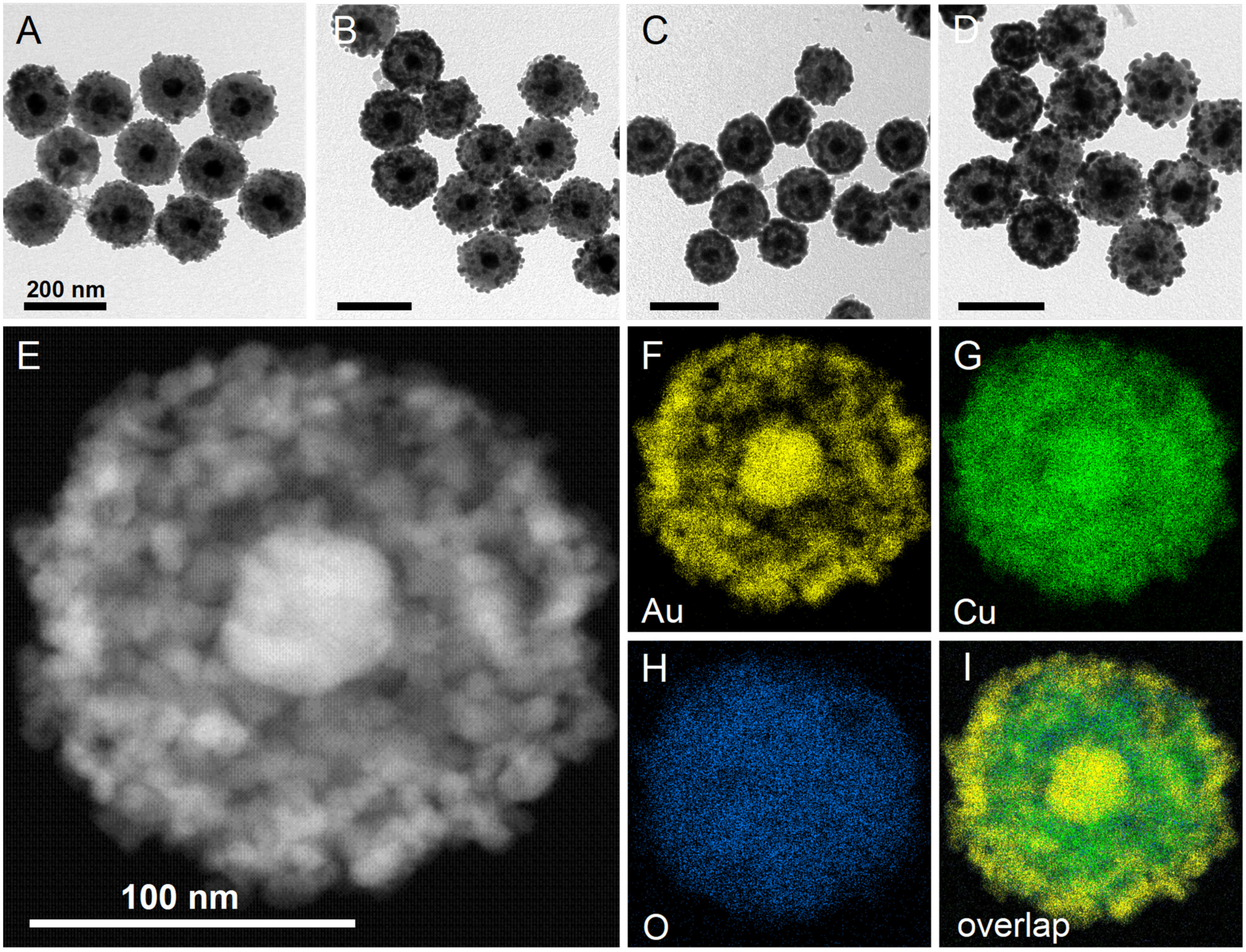

Figure S5. (A-D) TEM images of ACA NPs with varying amounts and tunable sizes of Au satellites by simply controlling the amount of $HAuCl_4$. (E-I) HAADF-STEM image and elemental maps of ACA NPs with small Au satellites. Scale bars: 200 nm.

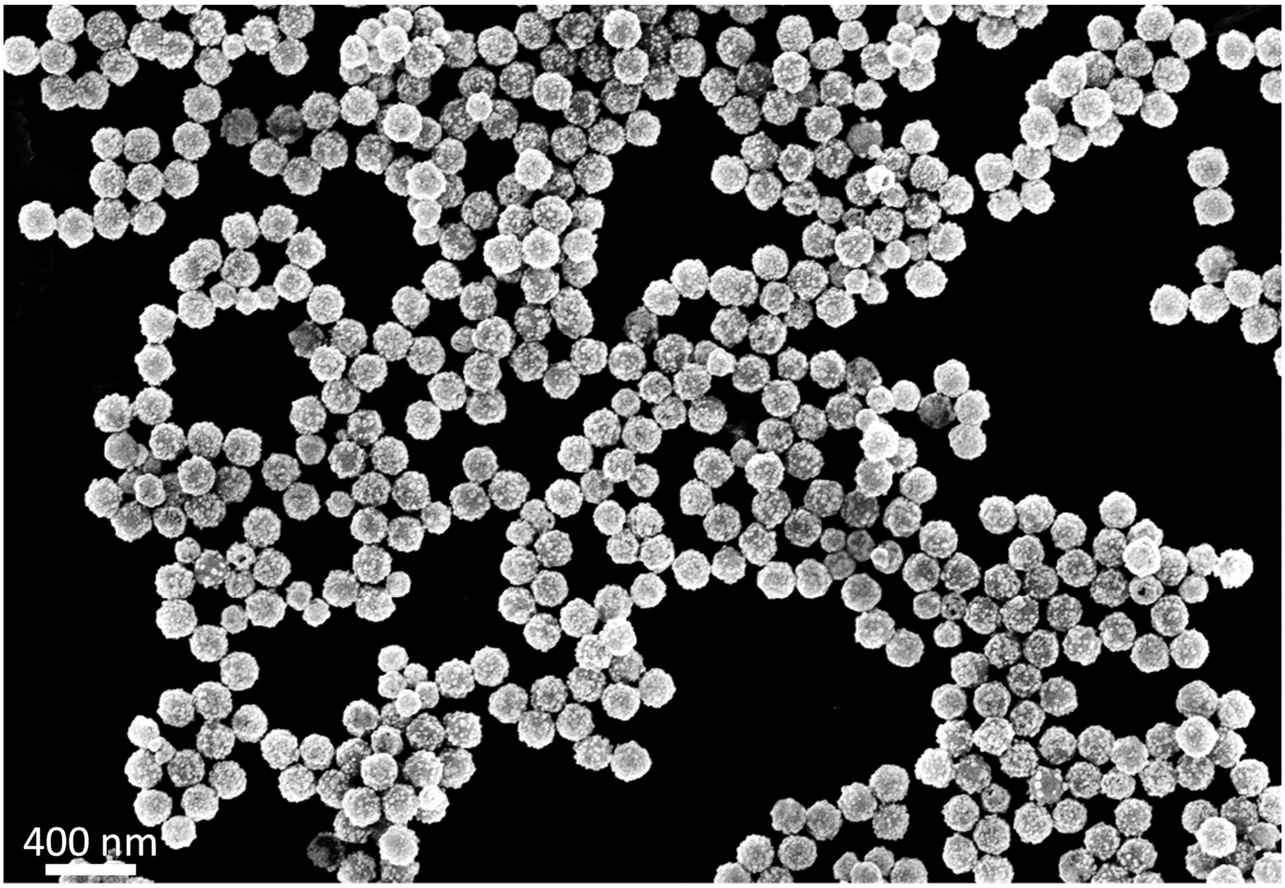

Figure S6. Low-magnification SEM image of ACA NPs.

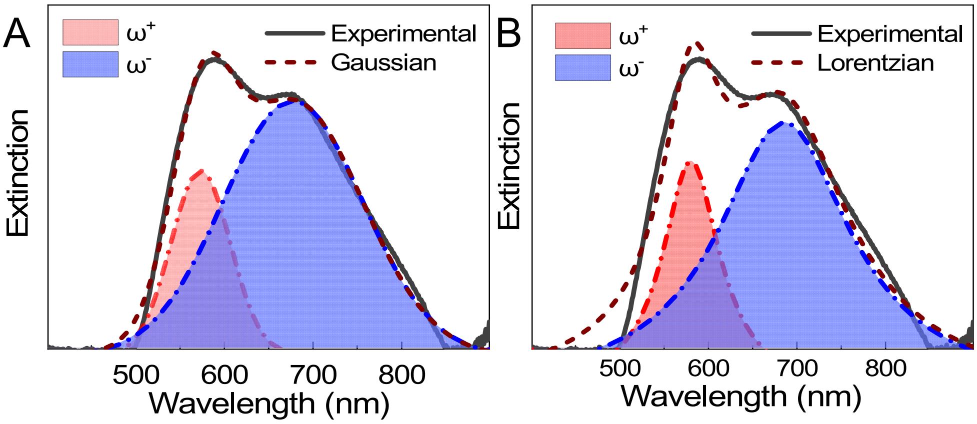

Figure S7. Extinction spectra of ACA NPs fitted by (A) Gaussian and (B) Lorentzian functions. The red and blue curves indicate the corresponding fitting of the dual extinction bands. The red-brown curves show the fitted results.

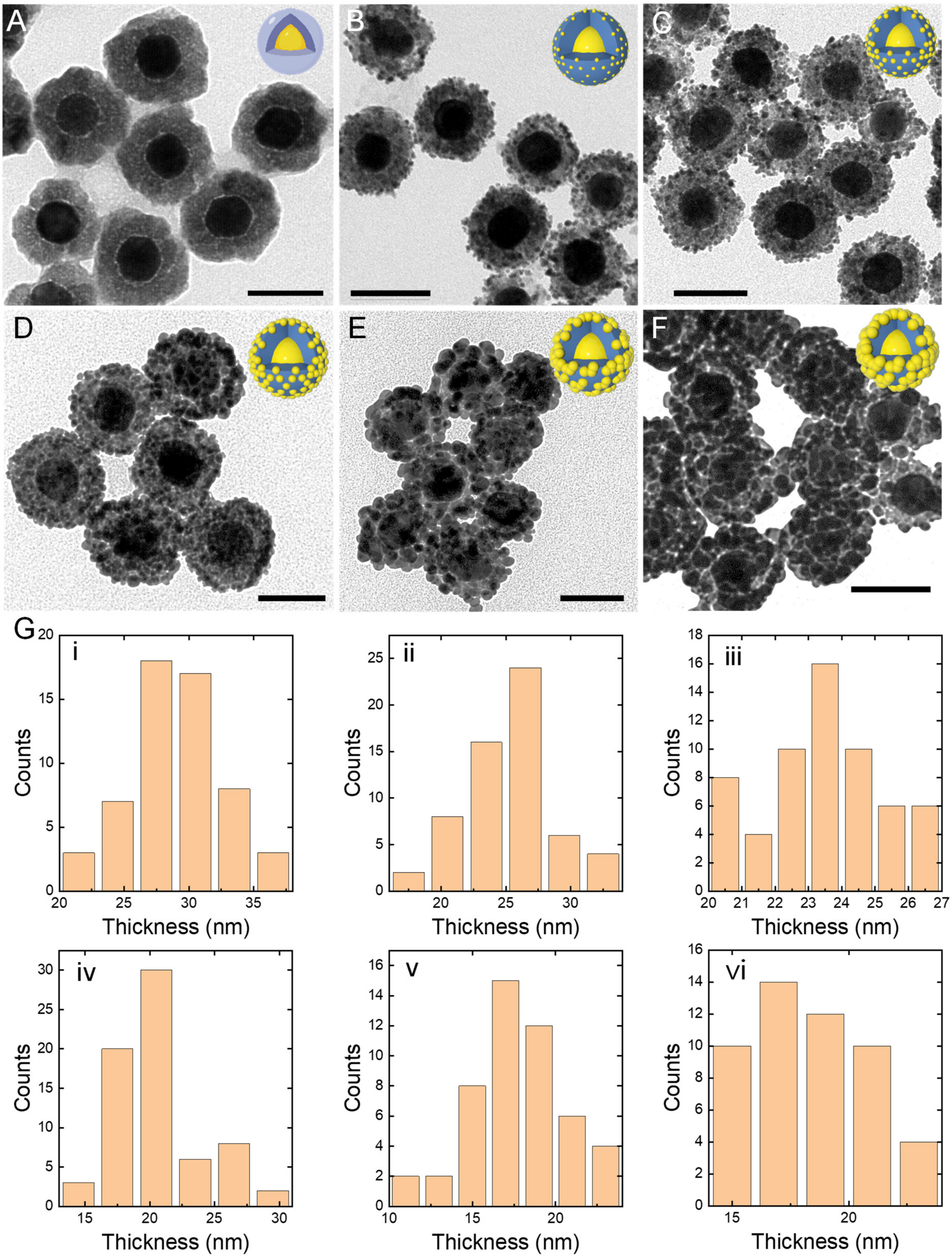

Figure S8. (A-F) TEM images of ACA NPs with distinct structures by controlling the size and density of Au satellites. The amount of Au precursor increases from panel A and panel F. The insets show the corresponding geometric models. Scale bars: 100 nm. (G) Histograms of the estimated Cu_2O thickness in ACA NPs.

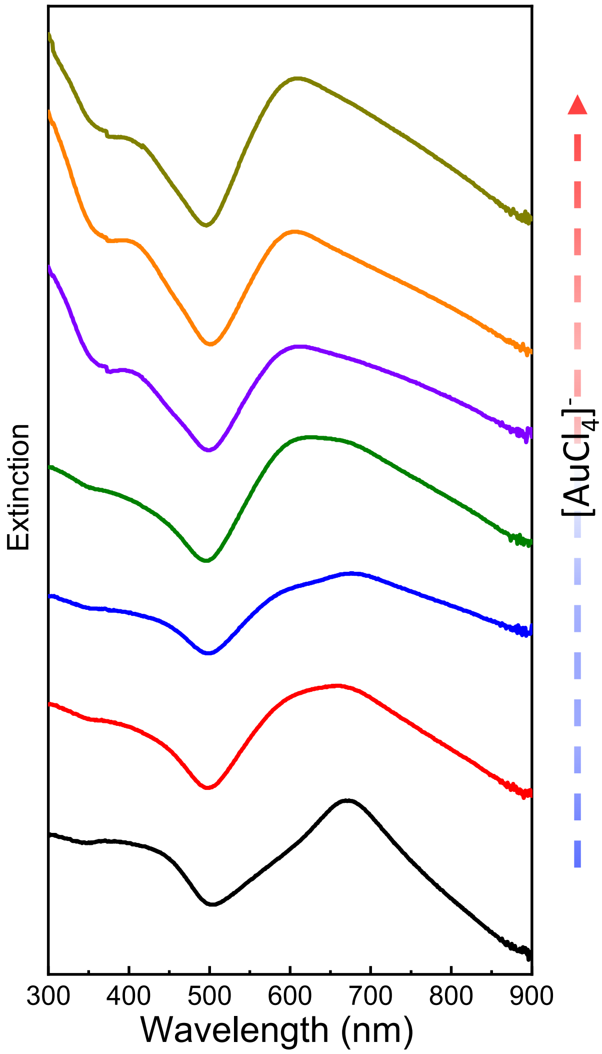

Figure S9. Extinction spectra of ACA NPs as a function of the amount of Au precursor during the transition from curve E to F in Figure 2A.

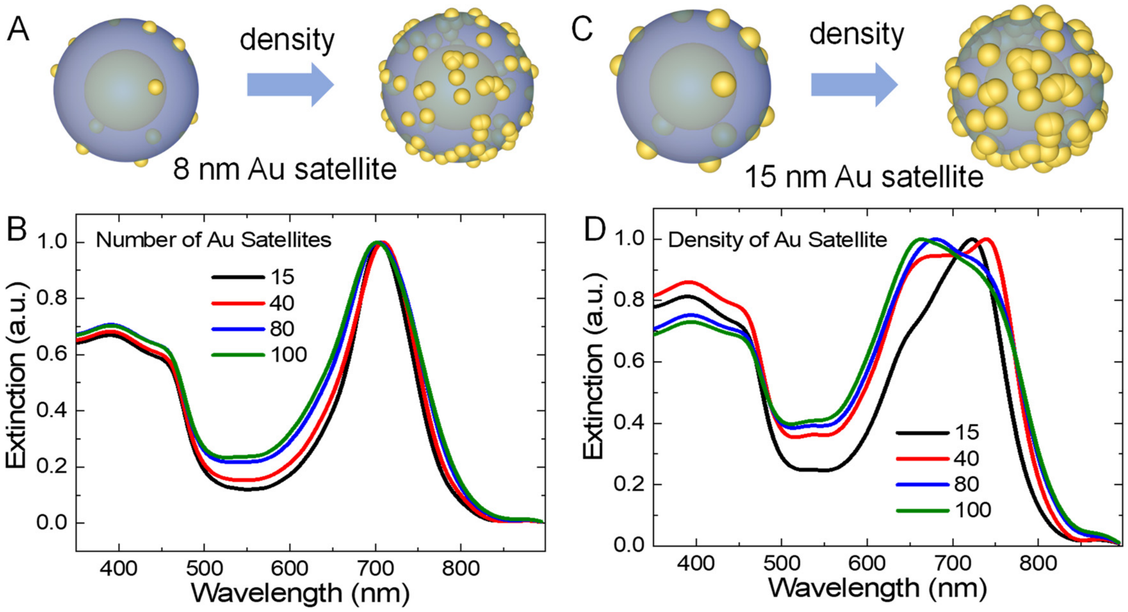

Figure S10. (A,C) Geometric models of ACA NPs with different densities of Au satellites (A: 8 nm and C: 15 nm in size). (B,D) Calculated extinction spectra of ACA NPs as a function of the density of Au satellites (B: 8 nm and D: 15 nm in size).

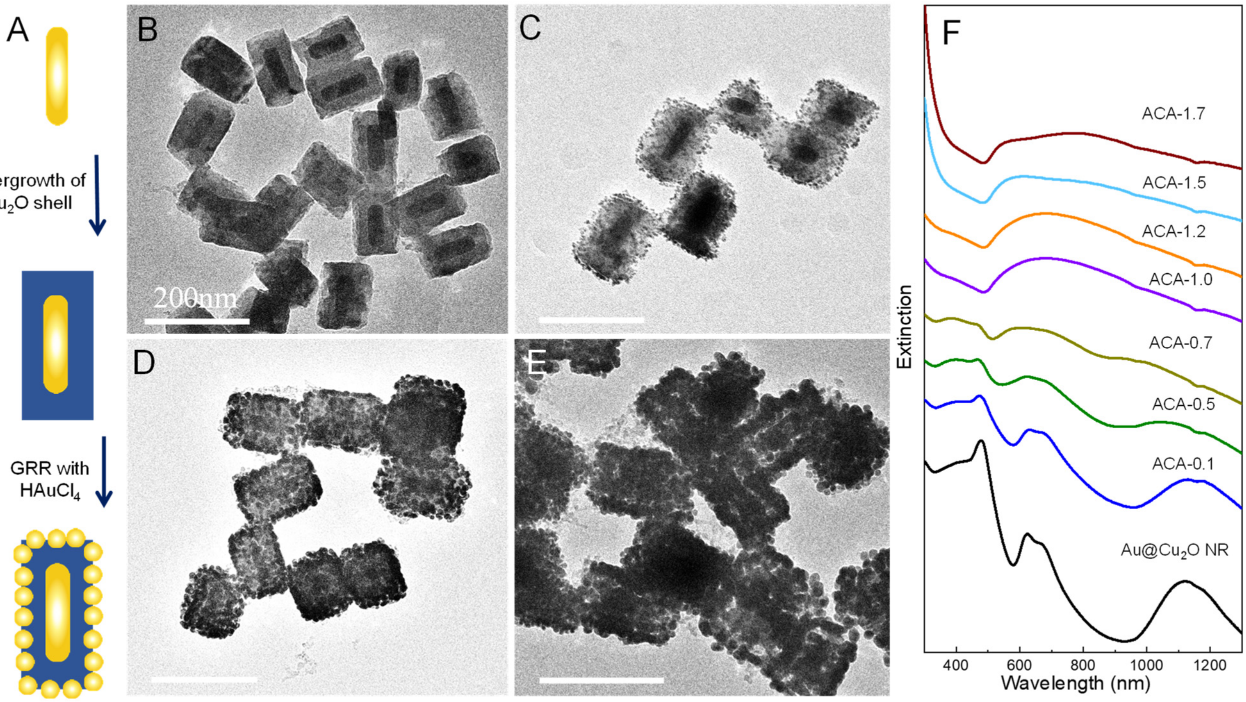

Figure S11. (A) Schematic illustration of the preparation of the ACA NRs. (B-E) SEM images of ACA NRs with varying sizes and densities of Au satellites prepared by varying the amount of Au precursors. (F) Optical extinction spectra of Au@Cu_2O NRs and corresponding ACA NRs formed through GRR between Cu_2O shell and $HAuCl_4$ with varying amounts.

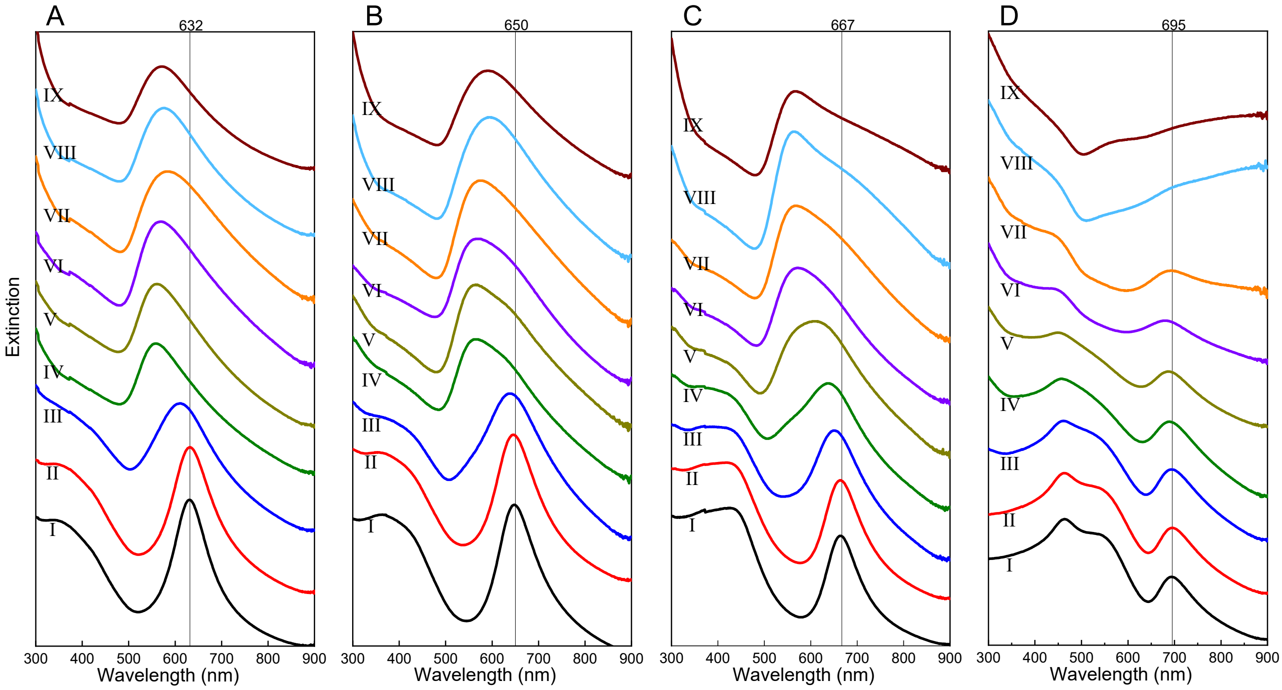

Figure S12. Optical extinction spectra of Au@Cu_2O NPs with different shell thicknesses (whose resonance wavelengths are located at 632, 650, 667, and 695 nm, respectively) and corresponding ACA NPs after the GRR process between Cu_2O shell with $HAuCl_4$ of different amounts, labeled as I, II, III, IV, V, VI, VII, VIII, and IX.

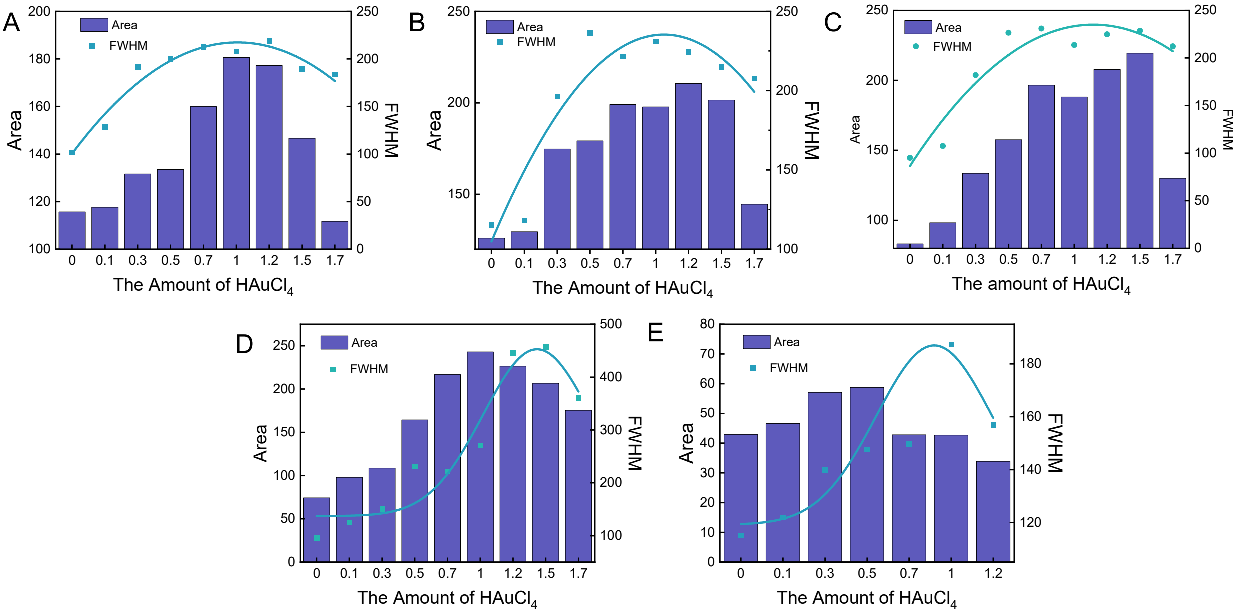

Figure S13. Histogram of FWHM and peak area (exacted from the extinction spectra shown in Figures S12A, S12B, S12C, 2A, and S12D, respectively) as a function of the amount of Au precursor.

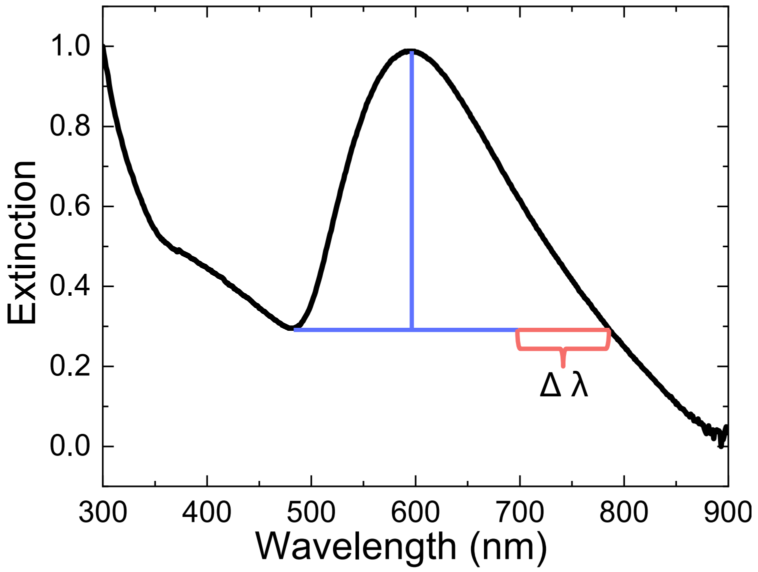

Figure S14. The definition of skewness is denoted as Δλ.

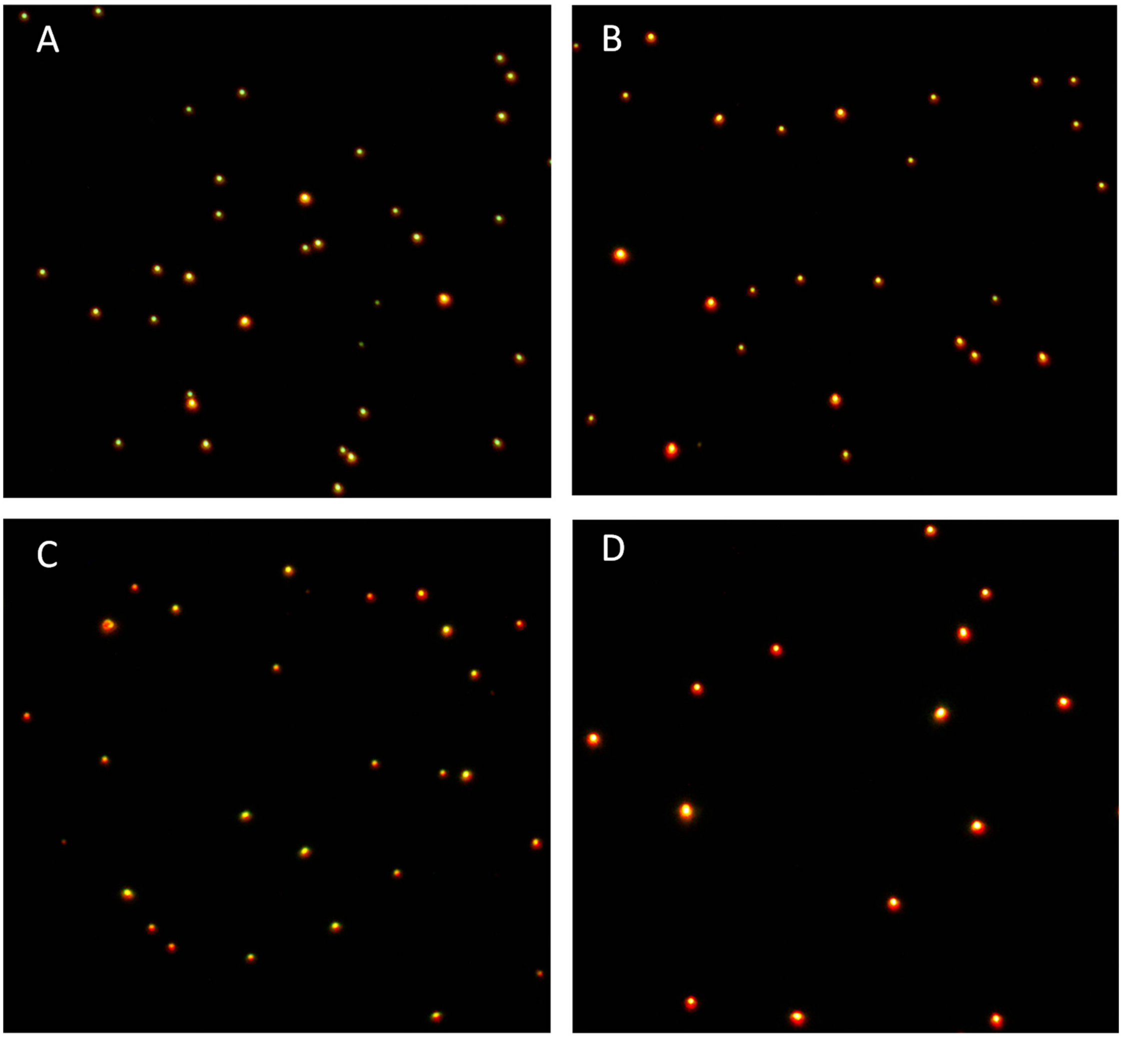

Figure S15. Single-particle dark field images of A (Au@Cu_2O@Au-0.1), B (Au@Cu_2O@Au-0.5), C (Au@Cu_2O@Au-1.0), and D (Au@Cu_2O@Au-1.5), respectively.

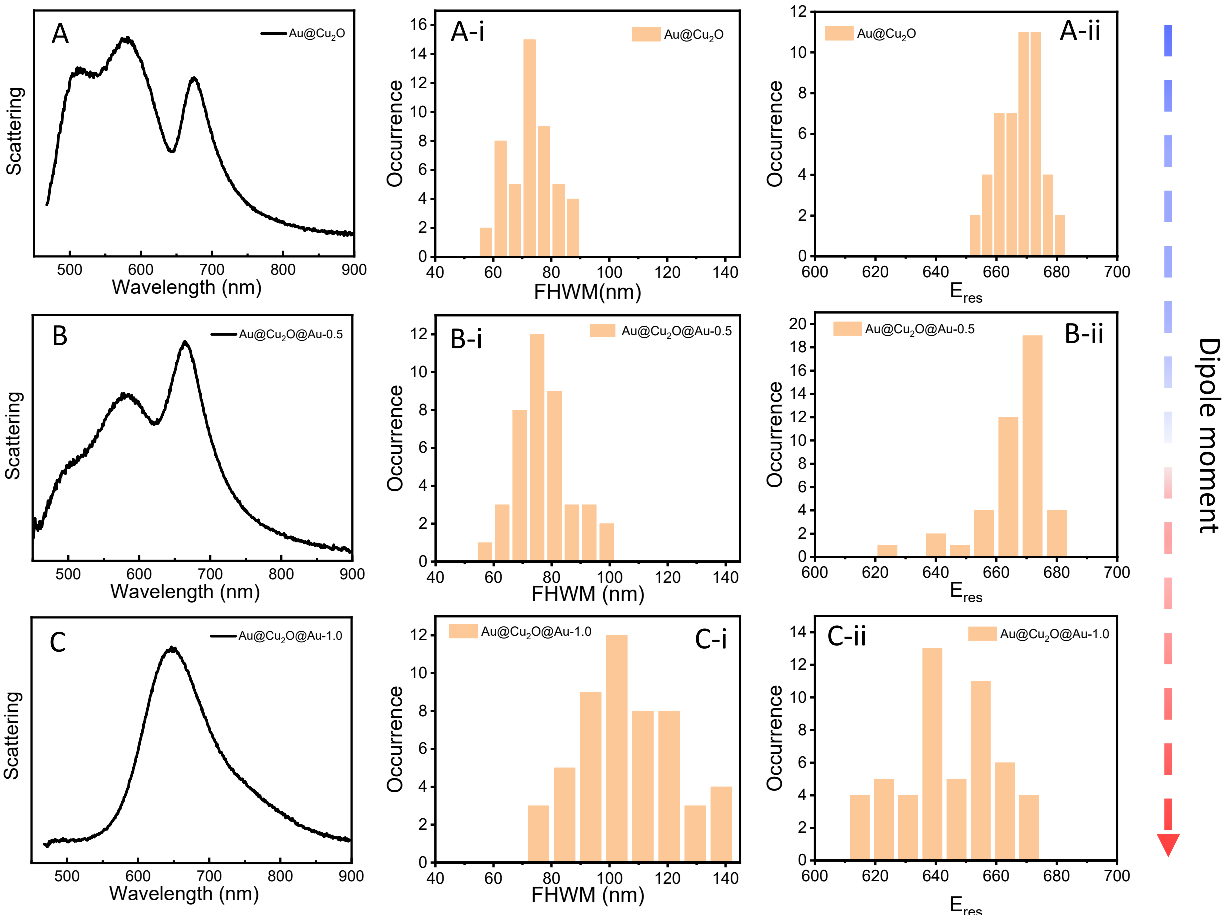

Figure S16. Single-particle scattering spectra of Au@Cu$_2$O (scattering peak at 670 nm) and corresponding ACA NPs after loading different sizes of Au satellites (Au@Cu$_2$O@Au-0.5 and Au@Cu$_2$O@Au-1.0). Statistical histogram of FWHM and *E$_{res}$* of corresponding samples on the left.

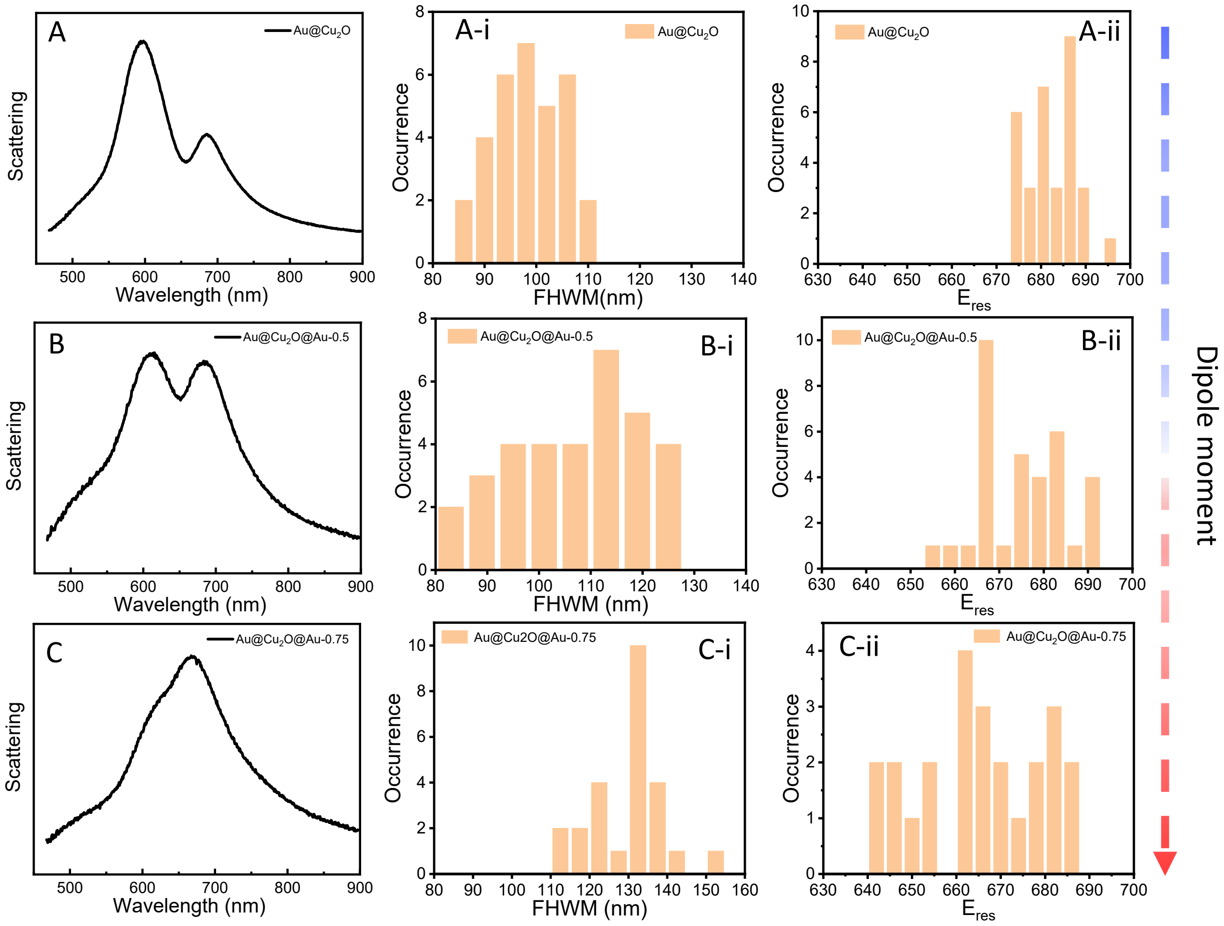

Figure S17. Single-particle scattering spectra of Au@Cu$_2$O (scattering peak at 688 nm) and corresponding ACA NPs after loading different sizes of Au satellites (Au@Cu$_2$O@Au-0.5 and Au@Cu$_2$O@Au-1.0). Statistical histogram of FWHM and E_{res} of corresponding samples on the left.

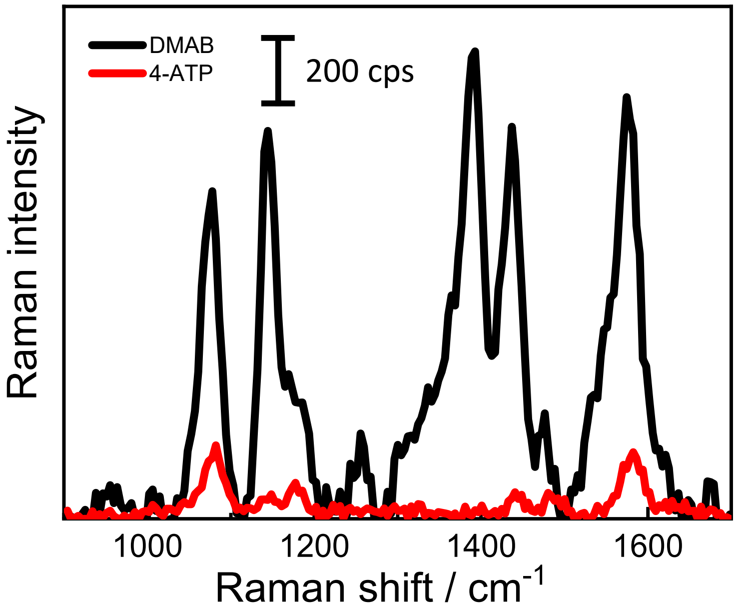

Figure S18. SERS spectra of 4-ATP and the corresponding DMAB on ACA NPs after laser excitations. The SERS pattern and relative peak intensity ratios of DMAB can be used to identify the conversion percentage of DMAB in the case of plasmon-driven dimerization of 4-NTP. The intensity ratio of the 1438 cm^{-1} mode to the 1572 cm^{-1} mode for DMAB on ACA NPs, denoted as R_{DMAB}, was used as an internal reference for the calculation of θ_{DMAB} at a reaction time, t.

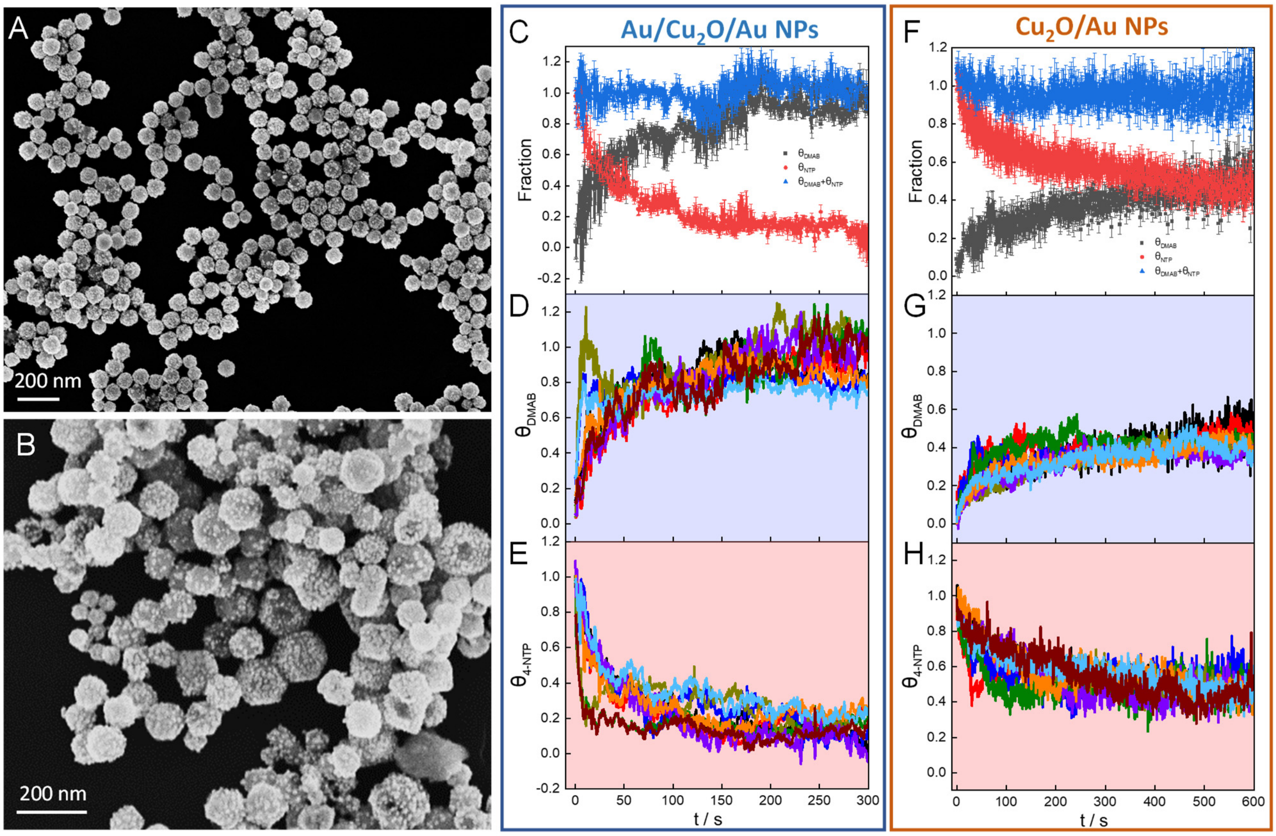

Figure S19. SEM images of (A) ACA NPs and (B) Cu$_2$O@Au NPs. (C) Ensemble-averaged θ_{NTP}, θ_{DMAB}, and $\theta_{DMAB} + \theta_{NTP}$ trajectories using ACA NPs. Trajectories of (D) θ_{DMAB} and (E) θ_{NTP} were collected on 8 individual 4-NTP-coated ACA NPs. (F) Ensemble-averaged θ_{NTP}, θ_{DMAB}, and $\theta_{DMAB} + \theta_{NTP}$ trajectories using Cu$_2$O@Au NPs. Trajectories of (G) θ_{DMAB} and (H) θ_{NTP} were collected on 10 individual 4-NTP-coated Cu$_2$O@Au NPs.

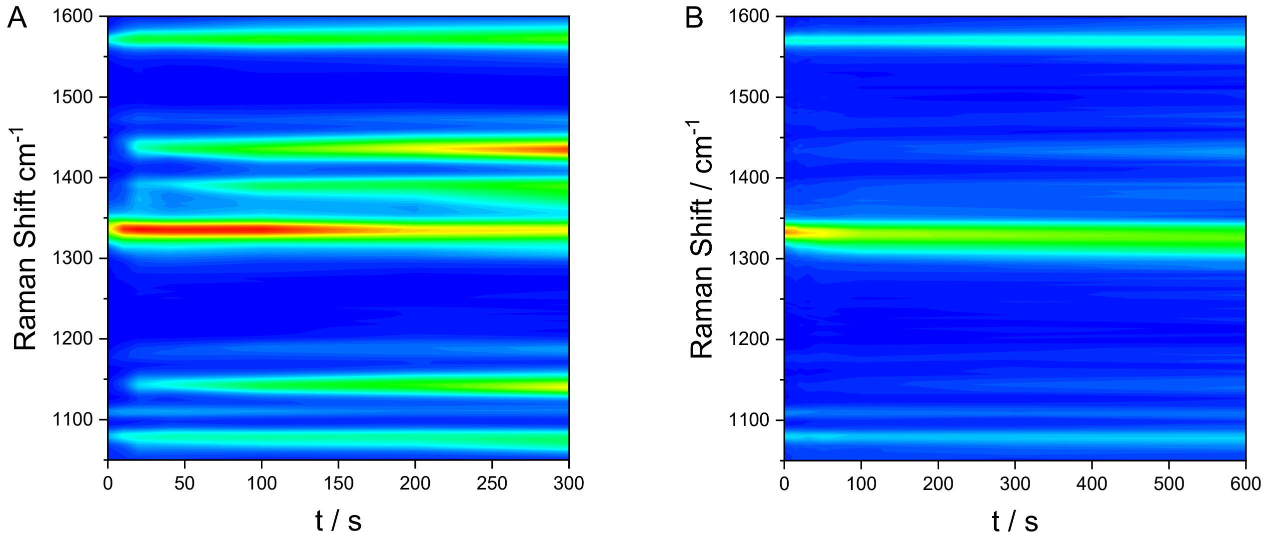

Figure S20. 2D map of time-resolved SERS spectra of 4-NTP upon 785 nm laser excitations using (A) ACA NPs and (B) Cu_2O@Au NPs, respectively.

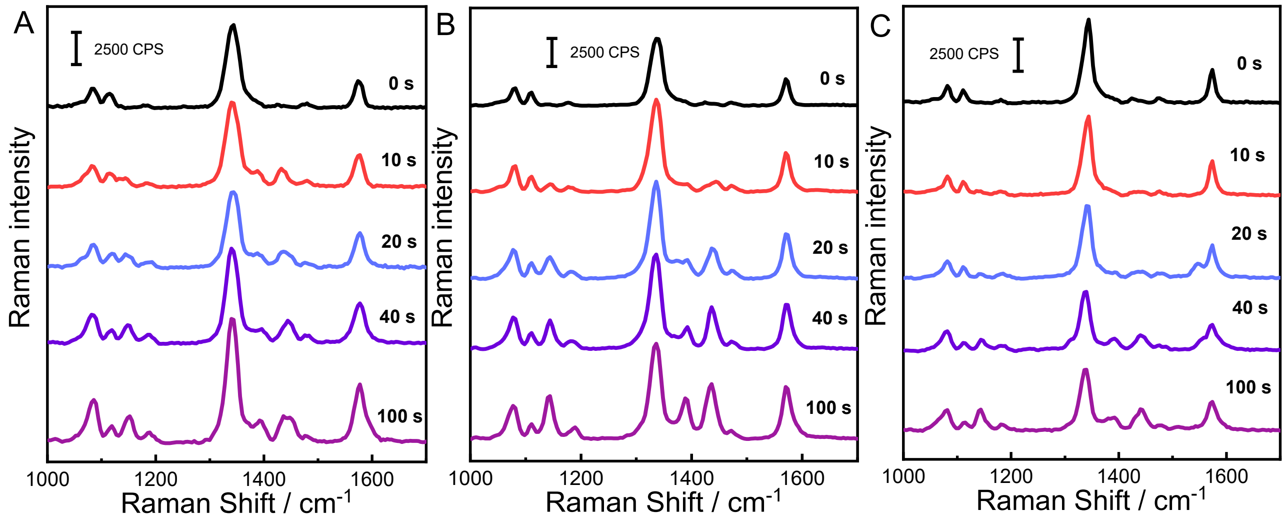

Figure S21. Time-resolved SERS spectra of 4-NTP on different ACA NPs upon 785 nm laser excitations. Panels A-C show ACA NPs with increases in sizes and densities of Au satellite tuned by increasing the amount of Au precursors during GRR. The results in panel B correspond to the results in Figure 5B.

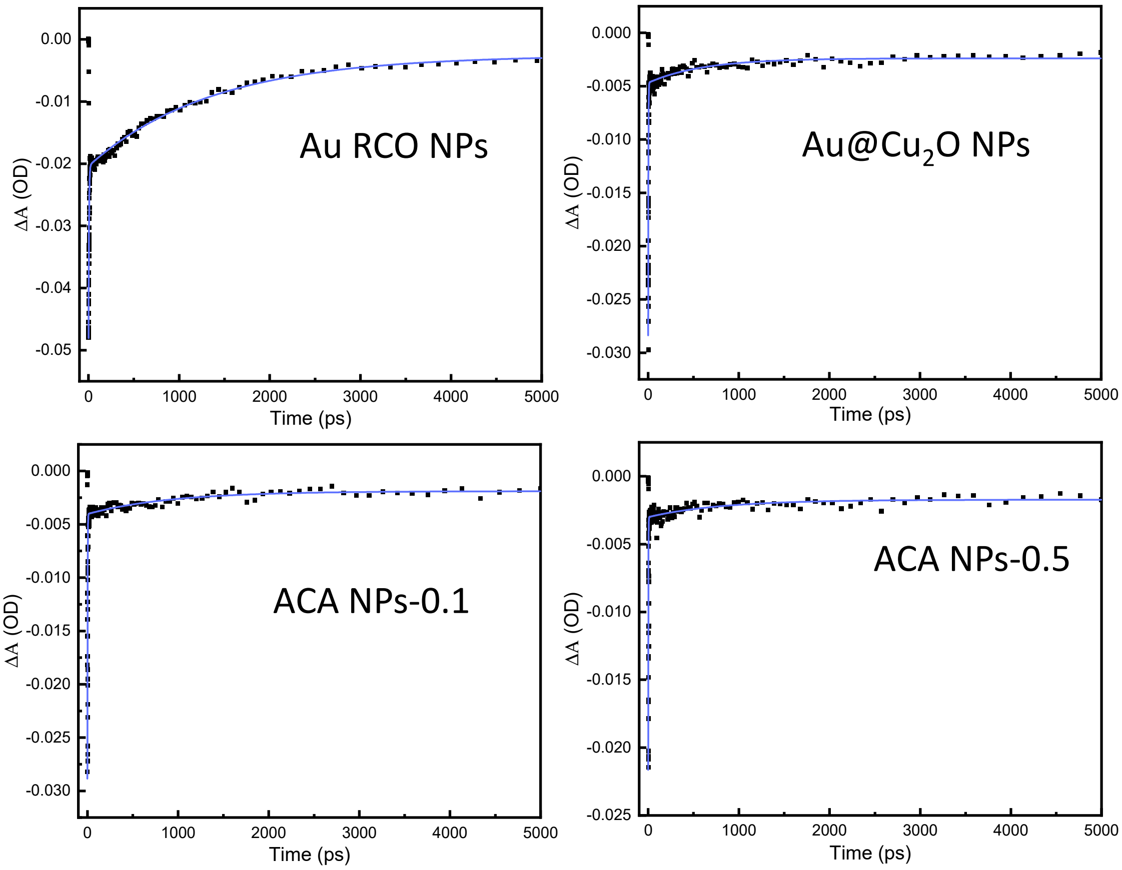

Figure S22. Ultrafast dynamics of the transient bleach of 4 different samples (Au RCO, Au@Cu$_2$O, ACA-0.1, ACA-0.5 NPs) at 532 nm, 657 nm, 657 nm, and 652 nm, respectively.

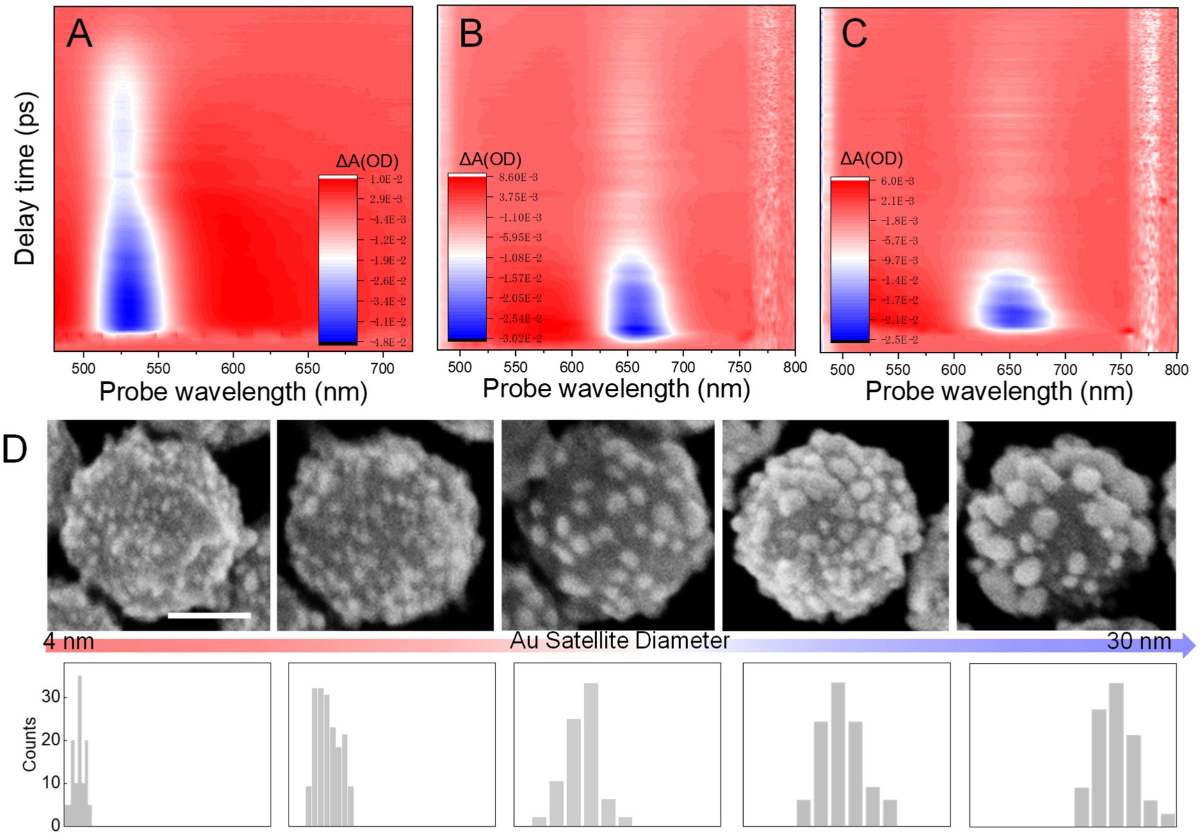

Figure S23. 2D maps of the TA spectra of (A) Au RCO NPs, (B) Au@Cu_2O NPs, (C) ACA NPs-0.5. Scale of the delay time: 35-200 ps. (D) SEM images and histograms show the variation of Au satellite diameter on the surface of Au@Cu_2O NPs as the amount of $HAuCl_4$ increases. Scale bar in panel D: 50 nm. All the SEM images share the same scale bar.

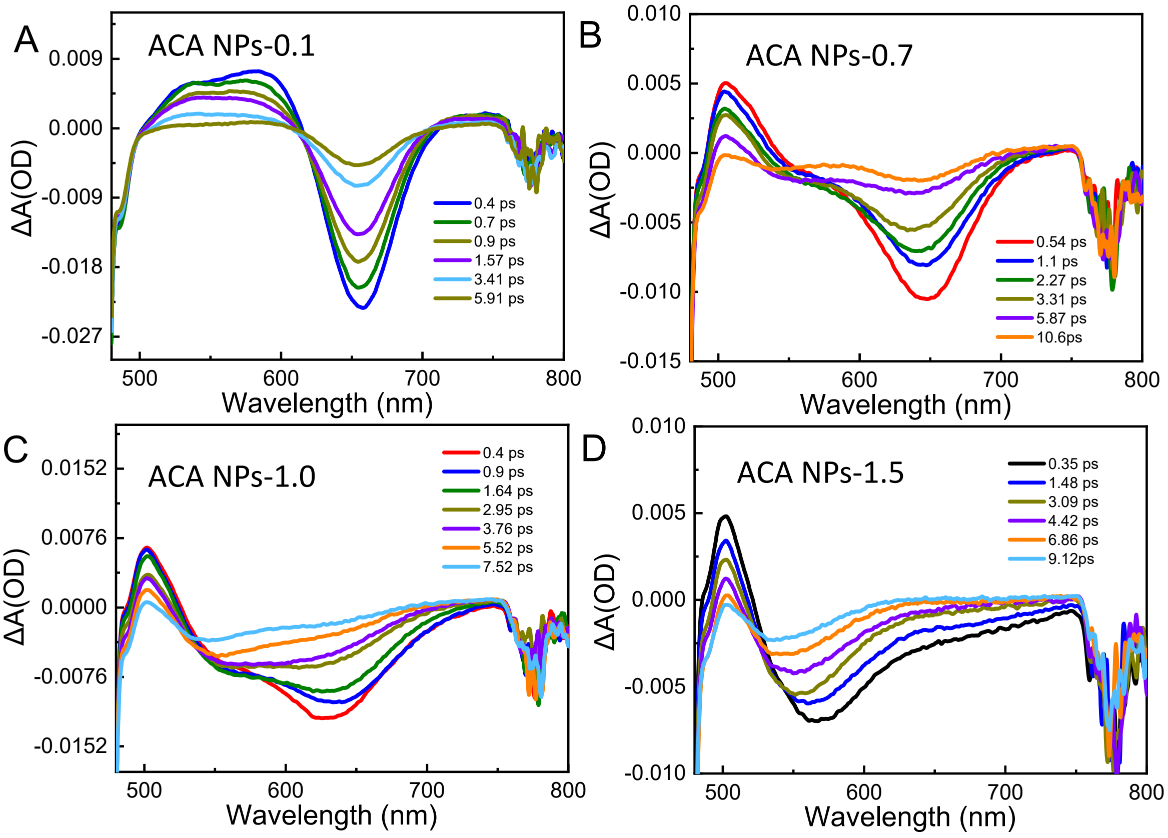

Figure S24. TA spectra of (A) ACA NPs-0.1, (B) ACA NPs-0.7, (C) ACA NPs-1.0, and (D) ACA NPs-1.5 after 450 nm excitation at various delay times. The suffix behind ACA NPs means different amounts of $HAuCl_4$ reacting with the $Au@Cu_2O$ NPs through GRR, which corresponds to the SEM images as shown in Figure S23D.

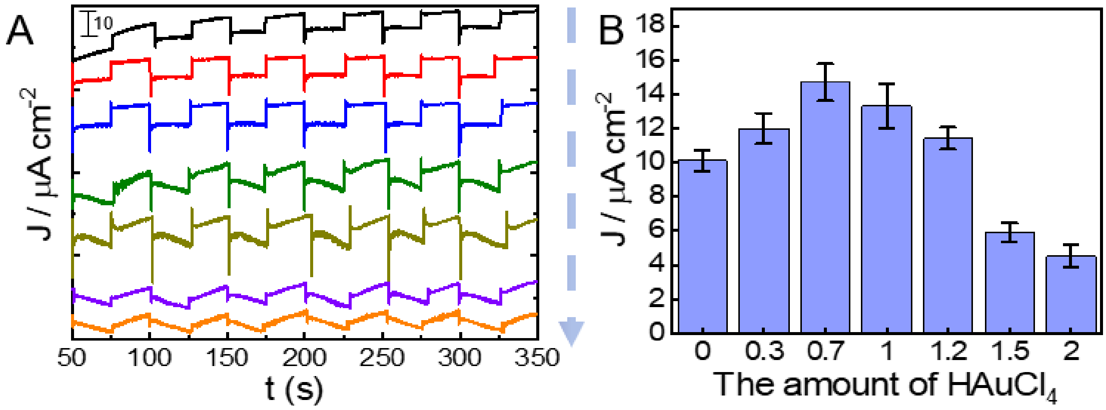

Figure S25. (A) Plots of photocurrent as a function of time for ACA NPs (Sample E in Figure S12) with different coupling conditions tuned by changing the amount of Au precursors according to light on/off at the same cathode applied potential (B) Histogram of photocurrents of ACA NPs with different coupling conditions tuned by changing the amount of Au precursors.

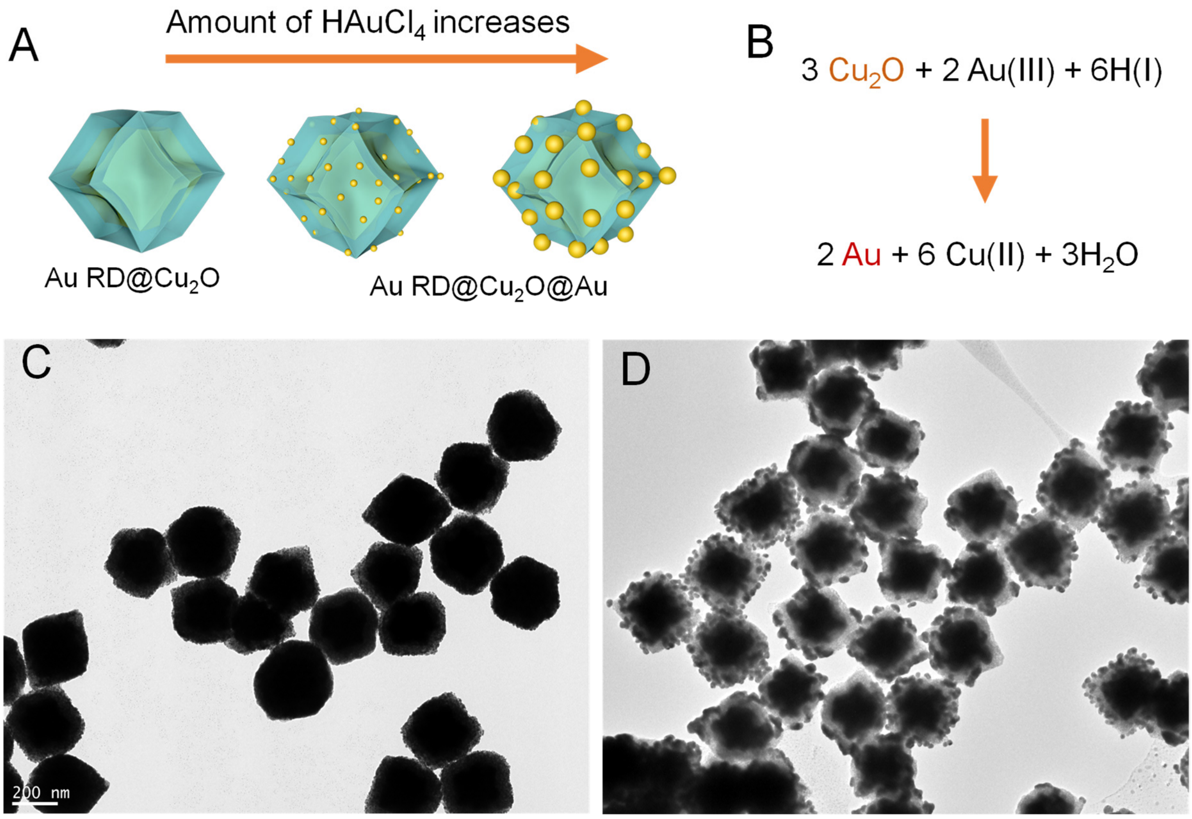

Figure S26. Construction and characterizations of chiral Au RD@Cu_2O@Au hybrid structures. (A) Schematic illustration of overgrowing Au NPs onto Au RD@Cu_2O NPs through the galvanic replacement reaction (GRR) between Au ions and Cu_2O shell as the amount of Au ions increases. (B) Chemical reaction formulas for GRR. (C-D) TEM images of Au RD@Cu_2O@Au NPs with different sizes of Au satellites. Note: the difference between Au RD@Cu_2O@Au NPs in panel C and panel D is that the amount of $HAuCl_4$ used in GRR is different. Panel D shares the same scale bar as panel D.

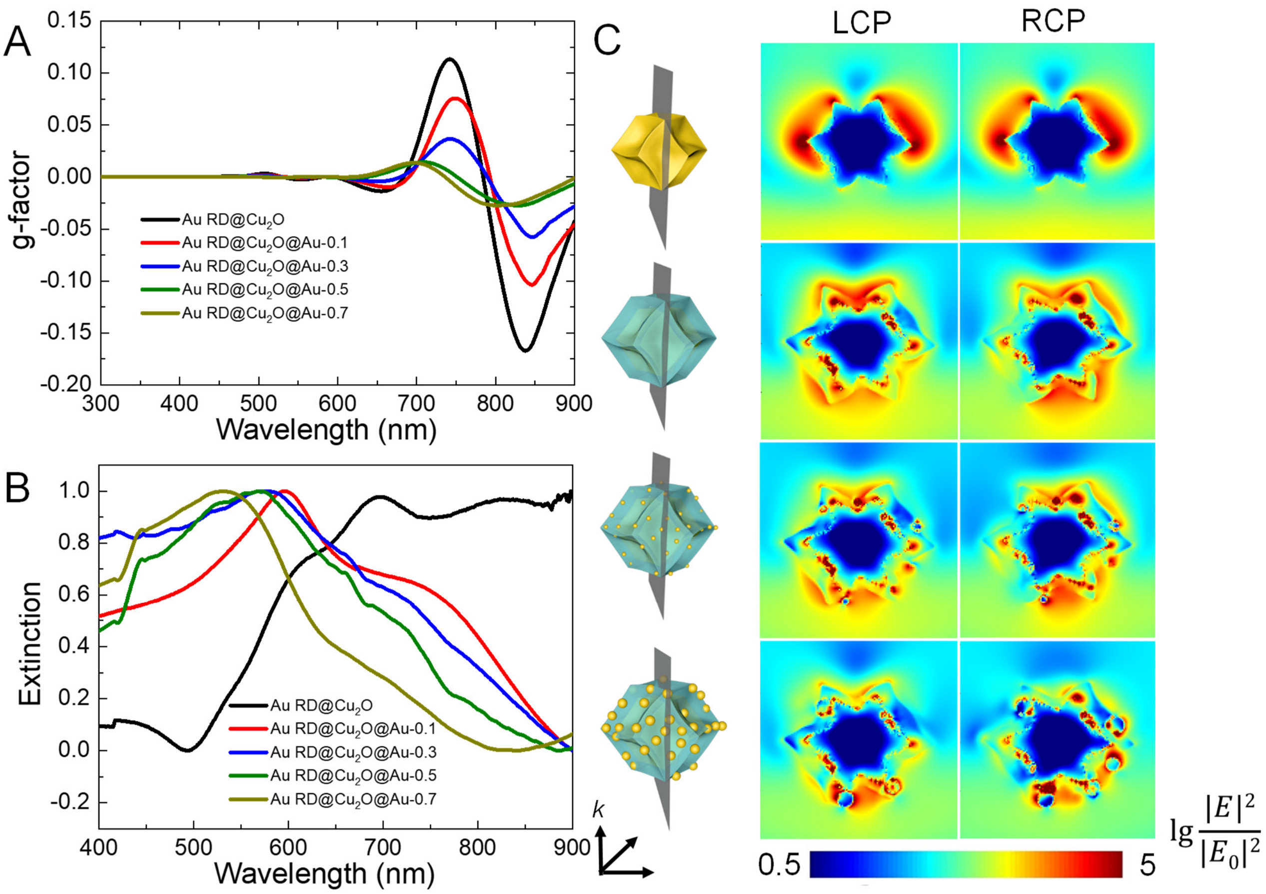

Figure S27. Optical properties of Au RD@Cu$_2$O@Au hybrid nanostructures. (A) The g-factor spectra of Au RD@Cu$_2$O@Au hybrid structures. The suffix behind Au RD@Cu$_2$O@Au NPs means different amounts of HAuCl$_4$ reacting with the Au RD@Cu$_2$O NPs through GRR. (B) Extinction spectra of Au RD@Cu$_2$O@Au hybrid structures. (C) Cross-sectional views of calculated near-field enhancements of Au RD, Au RD@Cu$_2$O, Au RD@Cu$_2$O@Au-I, and Au RD@Cu$_2$O@Au-II upon 824 nm LCP/RCP excitations, respectively. The field enhancements are plotted on a logarithm scale ($\lg|E/E_0|^2$). The corresponding geometries in three-dimensional Cartesian coordinates are illustrated, and one plane perpendicular to the incident plane wave *k* is shown. *k*: incident wave vector; LCP/RCP: left/right-handed circularly polarized light. Note: the difference between Au RD@Cu$_2$O@Au-I and Au RD@Cu$_2$O@Au-II is that the amount of HAuCl$_4$ used in GRR is different.

Table S1. Fitting parameters of LSPR bleach kinetics in Au, Au@Cu_2O, and ACA NPs with different sizes of Au satellites.

	τ_1 /ps	τ_2 /ps
Au NPs	4.89	1363±45
Au@Cu_2O NPs	2.45	605.41±108
ACA NPs-0.1	2.14	917±166
ACA NPs-0.5	1.65	812±202

S3. Supplementary References

[1] H. L. Wu, H. R. Tsai, Y. T. Hung, K. U. Lao, C. W. Liao, P. J. Chung, J. S. Huang, I. C. Chen, M. H. Huang, *Inorg. Chem.* **2011**, *50*, 8106-8111.

[2] X. C. Ye, C. Zheng, J. Chen, Y. Z. Gao, C. B. Murray, *Nano Lett.* **2013**, *13*, 765-771.

[3] Q. F. Zhang, L. L. Han, H. Jing, D. A. Blom, Y. Lin, H. L. L. Xing, H. Wang, *ACS Nano* **2016**, *10*, 2960-2974.

[4] X. Sun, J. Yang, L. Sun, G. Yang, C. Liu, Y. Tao, Q. Cheng, C. Wang, H. Xu, Q. Zhang, *ACS Nano* **2022**, *16*, 19174-19186.

[5] Q. Zhang, Y. Zhou, X. Fu, E. Villarreal, L. Sun, S. Zou, H. Wang, *J. Phys. Chem. C* **2019**, *123*, 26695-26704.

S4. Author Contributions

Q.Z., L.S., and Y.Y. conceived and designed the experiments. Y.Y., B.Z., X.S., Y.T., G.Y., Z.W., and C.L. performed the synthesis, analysis, and measurements. Y.Y., L.S., and Q.Z. co-wrote the paper. Q.Z. and L.S. supervised the entire study. All the authors contributed to the final version of the manuscript.